


## Original article

# Reactive transport modeling of water-CO<sub>2</sub>-rock interactions in clay-coated sandstones and implications for CO<sub>2</sub> storage

Huan Li<sup>1</sup>, Qinrong Hu<sup>2</sup><sup>\*</sup>, Rukai Zhu<sup>3</sup>, Bo Liu<sup>3</sup>, Achyut Mishra<sup>4</sup>, Eric O. Ansah<sup>5</sup>

<sup>1</sup>Hubei Key Laboratory of Complex Shale Oil and Gas Geology and Development in Southern China, Yangtze University, Wuhan 430100, P. R. China

<sup>2</sup>National Key Laboratory of Deep Oil and Gas, China University of Petroleum (East China), Qingdao 266580, P. R. China

<sup>3</sup>Xinjiang Research Institute of Huairou Laboratory, Urumqi 830000, P. R. China

<sup>4</sup>Department of Earth Sciences, Indian Institute of Technology Gandhinagar, Palaj, Gandhinagar, Gujarat 382355, India

<sup>5</sup>WH Bryan Mining & Geology Research Centre, Sustainable Minerals Institute, University of Queensland, Brisbane 4072, Australia

### Keywords:

CO<sub>2</sub> storage  
water-CO<sub>2</sub>-rock interactions  
grain-coating clay  
mineral carbonation  
mineral dissolution

### Cited as:

Li, H., Hu, Q., Zhu, R., Liu, B., Mishra, A., Ansah, E. O. Reactive transport modeling of water-CO<sub>2</sub>-rock interactions in clay-coated sandstones and implications for CO<sub>2</sub> storage. *Advances in Geo-Energy Research*, 2025, 17(2): 121-134.  
<https://doi.org/10.46690/ager.2025.08.04>

### Abstract:

In this work, the potential influences of grain-coating clays on water-CO<sub>2</sub>-rock interactions in sandstones and subsequent ramifications for CO<sub>2</sub> storage were investigated using reactive transport simulations. The results indicated that, compared to pore-filling smectite, grain-coating smectite leads to significant pH decrease, increases in the CO<sub>2</sub>-species concentrations, and decreases in smectite dissolution and the precipitation of secondary minerals. Moreover, it was revealed that smectite and chlorite coats dissolve preferentially over detrital K-feldspar being covered, while K-feldspar is dissolved preferentially over illite and kaolinite coats. While the mineral trapping mechanism is only important for smectite and chlorite coats, sandstone porosity is significantly reduced for chlorite coat but increased for the other three clay coats. The main causes of the differences between pore-filling and grain-coating scenarios for smectite and chlorite coats are ascribed to the inhibitory effect of clay coats on the growth of secondary quartz and the dissolution of clay. In addition to the above two factors, the decelerating effect of clay coats on the dissolution of K-feldspar is also important for illite coat; meanwhile, for the kaolinite coat, the dissolution of clay is less important and the other two factors are more critical. Furthermore, the coverage and thickness of clay coats, fluid flow rate, detrital grain size, detrital lithology, partial pressure of CO<sub>2</sub>, and temperature may all impact the role of clay coats.

## 1. Introduction

Many types of grain-coating clays have been observed (see the compilation by Li et al. (2024)), including chlorite, smectite, illite, kaolinite, and a mixture of multiple clays. In water-rock interactions, grain-coating clays have been suggested to decrease the available surface area of detrital grains, suppress the precipitation of secondary quartz (Worden et al., 2020; Gong et al., 2023), and retard the dissolution of

detrital feldspars being covered (Li et al., 2025). The inhibitory effect of clay coats on quartz cements has been regarded as a critical mechanism responsible for the preservation of sandstone porosity at deep burial depths (Walderhaug and Porten, 2022).

Regarding the decelerating effect of clay coats on the dissolution of detrital feldspars being covered, different scholars hold different viewpoints. On one hand, some studies have suggested that grain-coating minerals hardly affect the disso-

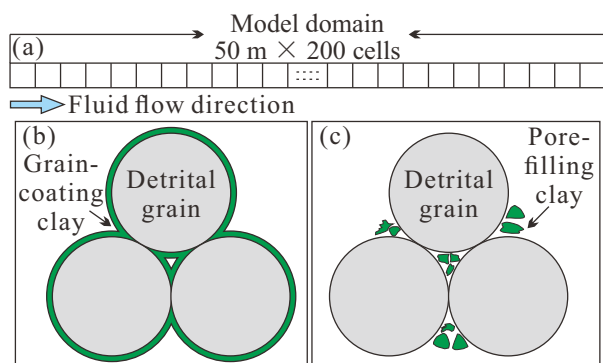


**Fig. 1.** (a) One-dimensional homogeneous reactive transport model domains and (b) grain-coating and (c) pore-filling clay minerals.

lution rates of the minerals being covered. For example, Hodson (2003) conducted flow-through dissolution experiments to react anorthite powder with  $\text{FeCl}_3$  and  $\text{HCl}$  solutions at a pH of 2.6 and a temperature of 25 °C, and observed that the precipitation of amorphous Fe-rich coatings in the  $\text{FeCl}_3$  solution did not apparently decelerate the steady-state dissolution rate of anorthite compared to the dissolution rate in  $\text{HCl}$  solution. Meanwhile, others suggested that grain-coating minerals are able to significantly slow the dissolution rates of the minerals being covered because they can decrease the available surface area of these minerals (Daval et al., 2009) and reduce the mass diffusion rate across the coating phase (Li et al., 2025). In fact, the dissolution rate reduction degree is collectively controlled by the coverage, thickness and microporosity of the coating phase (Emmanuel, 2022). Therefore, it is likely that the conclusion from Hodson (2003) is caused by the very low coverage of Fe-rich coatings, as illustrated by scanning electron microscopy images.

In geological  $\text{CO}_2$  storage, injected  $\text{CO}_2$  can reduce water pH through the formation of  $\text{HCO}_3^-$ , react with *in-situ* primary minerals, and precipitate secondary minerals (Kharaka et al., 2006). Clay coats such as chlorite and smectite are typically rich in Fe, Mg and Ca (McKinley et al., 2003). The dissolution of these Fe-Mg-Ca-rich clay coats under  $\text{CO}_2$ -rich fluid conditions may precipitate secondary carbonate minerals (Luquot et al., 2012) and enhance the mineral carbonation of  $\text{CO}_2$ . In summary, the aforementioned properties of grain-coating clays may significantly change the geochemical reactions among water,  $\text{CO}_2$  and sandstone minerals, and eventually altering the fate of injecting  $\text{CO}_2$ . However, the complex influences of grain-coating clays remain largely underexplored.

To address these unanswered questions, this study investigates the influences of grain-coating clays on  $\text{CO}_2$  storage in sandstones via reactive transport simulations while considering real geological conditions for model setup. The objective is to preliminarily explore the influences of grain-coating clays on  $\text{CO}_2$  storage and provide foundations for future studies regarding water- $\text{CO}_2$ -rock interactions in clay-coated sandstones.

## 2. Numerical models

### 2.1 Overview

The simulator Geochemist's Workbench<sup>®</sup> 13.0 Pro (GWB) was employed to construct one dimensional, horizontal and homogeneous models involving clay coats. The numerical models are 50 m in length discretised into 200 cells (Fig. 1), which results in a uniform cell size of 0.25 m.

Different petrographic and geochemical parameters were considered:

- 1) Different thicknesses of clay coat (4, 8, 12, 16 and 20  $\mu\text{m}$ ), were tested in a range corresponding to the measured coat thickness values in natural samples (Worden et al., 2020; Li et al., 2024);
- 2) Different coverages of clay coats (20%, 40%, 60%, 80% and 100%) were introduced into the model;
- 3) Four grain sizes (0.04, 0.2, 0.4 and 1 mm) were considered to calculate the clay coat volume in siltstone, fine sandstone, medium sandstone, and coarse sandstone;
- 4) Four types of grain-coating clays (chlorite, smectite (saponite-Ca), illite (muscovite used as a proxy), and kaolinite) were set;
- 5) Three detrital sandstone lithologies (quartz arenite, subarkose and arkose) (Folk, 1974), were considered by changing the proportions of detrital quartz and K-feldspar;
- 6) Multiple  $p\text{CO}_2$  values (2, 4, 6, 8 and 10 MPa) were used to represent different concentrations of the injected  $\text{CO}_2$  gas;
- 7) Different formation temperatures (60, 70, 80, 90 and 100 °C), were used to represent a range of burial depths of sandstone formations used for  $\text{CO}_2$  storage (Metz et al., 2005);
- 8) Three fluid velocities (0.1, 1 and 10 m/yr) were tested considering the gas-injection rate, variation in flow velocity in the near- and far from well borehole environments, and the evaluation of natural fluid flow velocities in subsurface formations (Giles, 1987).

In order to highlight the influence of grain-coating clay minerals on  $\text{CO}_2$  storage, a counterpart scenario of pore-filling (non-coating) clay mineral was also presented for comparison (Fig. 1). In this scenario, the same clay volume was used as in the grain-coating scenario. There are two differences in the model settings between the two scenarios: The detrital quartz surface area and K-feldspar dissolution rate are mathematically decreased in the grain-coating scenario, while they are not in the pore-filling scenario.

### 2.2 Thermodynamic dataset

The Lawrence Livermore National Laboratory dataset was consistently employed as the thermodynamic dataset used in the constructed models (Delany and Lundeen, 1990). The calculation of activity coefficients of aqueous component is achieved through Debye-Hückel equation (Helgeson, 1969).

## 2.3 Mineralogy

In conceptual models, the sandstones are composed of detrital quartz, detrital K-feldspar, clay coat, and porosity. Prior to the involvement of clay coat, the detrital grains were set as 70 vol.% and the initial porosity as 30 vol.%. Three sandstone lithologies were considered: Quartz arenite consisting of 65% quartz and 5% K-feldspar, sub-arkose consisting of 55% quartz and 15% K-feldspar, and arkose consisting of 45% quartz and 25% K-feldspar. The volume of grain-coating clay was mathematically calculated (Section 2.4) and the porosity was reduced accordingly.

Saponite-Ca [ $\text{Ca}_{0.165}\text{Mg}_3\text{Al}_{0.33}\text{Si}_{3.67}\text{O}_{10}(\text{OH})_2$ ] was selected as a representative of trioctahedral smectite (Table S1), which is the typically observed smectite type in clastic sediments (McKinley et al., 2003). Muscovite [ $\text{KAl}_3\text{Si}_3\text{O}_{10}(\text{OH})_2$ ] was used to represent illite. The formula of chlorite (clinocllore<sub>0.5</sub>daphnite<sub>0.5</sub>;  $\text{Mg}_{2.5}\text{Fe}_{2.5}\text{Al}_2\text{Si}_3\text{O}_{10}(\text{OH})_8$ ) and the thermodynamic data were manually composed using daphnite and clinocllore (Li et al., 2024). Magnesite, siderite and dolomite were selected as secondary minerals (Table S1) considering the reaction pathway model results (Section 3.1).

## 2.4 Clay volume

The calculation of the volume content of clay coat ( $V$ ) employs a method involving the calculation of the specific surface area ( $S$ ) of consolidated sandstones (Li et al., 2024):

$$V = \frac{4.23(1-\phi)^2}{d} Ch(1-\phi_c) \quad (1)$$

where  $\phi$  denotes sandstone porosity without involving grain-coating clays,  $d$  denotes median grain size,  $C$  denotes the coverage of clay coats,  $h$  denotes the thickness of clay coats, and  $\phi_c$  denotes the intergranular microporosity of grain-coating clays. The thickness of grain-coating clay was set to be consistent in every model (Fig. 1). The reported averaged intergranular microporosities of chlorite, illite, and smectite are  $\sim 50\%$  (Hurst and Nadeau, 1995),  $\sim 35\%$  (Alansari et al., 2019), and  $\sim 15\%$  (Alansari et al., 2019), respectively. However, to our knowledge, the microporosity of kaolinite coat has not been measured and reported. Thus, this study used the reported microporosity of pore-filling kaolinite (average:  $\sim 45\%$ ) as an alternative (Alansari et al., 2019).

## 2.5 Dissolution-precipitation kinetics

### 2.5.1 Kinetic rate laws

In light of the transition state theory, mineral reaction behaviours can be constrained as (Lasaga, 2014):

$$r = -S'k_+f(a_i)g(\Delta G) \quad (2)$$

where  $r$  denotes the reaction rate describing the dissolution or precipitation of a mineral and  $S'$  denotes the bulk surface area of the considered mineral. The term  $k_+$  denotes the reaction rate constant, which can be estimated by (Lasaga, 2014):

$$k_+ = k_{25^\circ\text{C}} \exp \left[ \frac{-E}{R} \left( \frac{1}{T} - \frac{1}{298.15} \right) \right] \quad (3)$$

where  $k_{25^\circ\text{C}}$  denotes the reaction rate constant at a condition of  $25^\circ\text{C}$ ,  $E$  denotes the activation energy of the considered mineral,  $R$  denotes the universal gas constant, and  $T$  denotes the Kelvin temperature. The term  $g(\Delta G)$  is estimated using the relationship with the saturation index of the mineral (Lasaga, 2014):

$$g(\Delta G) = \left[ 1 - \left( \frac{Q}{e} \right)^{p_i \gamma^{q_i}} \right] \quad (4)$$

where  $Q$  denotes the activity product of species involved in the reaction,  $e$  denotes the equilibrium constant, and  $p_i$  and  $q_i$  denote empirical constants. The term  $f(a_i)$  explains the promoting or inhibitive effects of a specific species  $i$  and is calculated considering the exponential relationship ( $n_i$ ) with the activity ( $a_i$ ) of the involved aqueous species  $i$  as follows (Oelkers et al., 1994):

$$f(a_i) = \prod_i a_i^{n_i} \quad (5)$$

Proton ( $\text{H}^+$ ) is typically the dominant species that impact reaction rate for most minerals (Palandri and Kharaka, 2004). The activity of  $\text{H}^+$  can be incorporated into the rate equation, integrating three mechanisms at acid, near neutral and alkaline solution conditions (Palandri and Kharaka, 2004):

$$r = S' \left[ \begin{array}{l} k_a^{25^\circ\text{C}} \exp \left[ \frac{-E_a}{R} \left( \frac{1}{T} - \frac{1}{298.15} \right) \right] a_{\text{H}^+}^n \\ + k_n^{25^\circ\text{C}} \exp \left[ \frac{-E_n}{R} \left( \frac{1}{T} - \frac{1}{298.15} \right) \right] \\ + k_b^{25^\circ\text{C}} \exp \left[ \frac{-E_b}{R} \left( \frac{1}{T} - \frac{1}{298.15} \right) \right] a_{\text{H}^+}^m \end{array} \right] \left[ 1 - \left( \frac{Q}{K} \right)^{p \gamma^q} \right] \quad (6)$$

where  $k_a^{25^\circ\text{C}}$ ,  $k_n^{25^\circ\text{C}}$ , and  $k_b^{25^\circ\text{C}}$  stand for the standard rate constants under acid, neutral and alkaline conditions, respectively;  $E_a$ ,  $E_n$ , and  $E_b$  stand for the activation energy under acid, neutral and alkaline conditions, respectively;  $a_{\text{H}^+}$  denotes the activity of aqueous proton ( $\text{H}^+$ );  $n$  and  $m$  stand for exponential orders of the activity of  $\text{H}^+$  under acid and alkaline conditions, respectively. The  $k_{25^\circ\text{C}}$ ,  $E$ ,  $n$ , and  $m$  values of quartz, K-feldspar, siderite, chlorite, illite, magnesite, smectite, kaolinite, and dolomite were directly sourced from Palandri and Kharaka (2004) (Table S1). Moreover, nucleus density was employed in the GWB as the original surface area of a mineral that is not present in the original model (Bethke, 2008). In this study, a nucleus density of  $10 \text{ cm}^2/\text{cm}^3$  for non-clay minerals was artificially selected, including magnesite, siderite and dolomite. The nucleus density of kaolinite was artificially set to  $100 \text{ cm}^2/\text{cm}^3$  (Table S1) (Bethke, 2008).

Specific surface area is a pivotal parameter in evaluating and predicting mineral reaction rates (Eq. (2)). Beckingham et al. (2016) suggested that the 2D image-based specific surface area could derive an effluent concentration most closely matching their flow-through experimental results. Therefore, the available two-dimensional image-based  $S$  values measured by Beckingham et al. (2016) were applied, including quartz, K-feldspar, kaolinite, chlorite, and smectite. The specific surface area of illite (Lammers et al., 2017), siderite (Golubev et

al., 2009), magnesite (Pokrovsky et al., 2009), and dolomite (Luhmann et al., 2014) were reported in their respective artificial dissolution experiments and utilized in this work (Table S1).

As the effective surface area ( $S_E$ ) in natural environments is typically larger than the measured values, this may lead to overestimated reaction rates (Beckingham et al., 2017). This effect can be overcome through a scaling factor ( $F$ ) to manually decrease the measured  $S$  ( $S_E = S \times F$ ). Following the practice of Beckham et al. (2017), a  $F$  of  $10^{-2}$  and  $10^{-5}$  were uniformly employed for minerals, of which the volume contents were greater and smaller than 5 vol.%, respectively.

Moreover, it has been observed that the mineral dissolution rate significantly decreases with the reaction approaching equilibrium (Black and Haese, 2014; Lasaga, 2014). To address this issue, it has been suggested that the second-order rate law can be sufficiently satisfied in overcoming the overestimated reaction rate under close-to-equilibrium conditions (Bethke, 2008). To achieve this,  $p$  was manually set as 1 and  $q$  was set as 2 following the practice by Bethke (2008).

### 2.5.2 Inhibition of secondary quartz

Previous studies mainly used the following equation to achieve the inhibitory effect of clay coats on secondary quartz (Lander and Walderhaug, 1999):

$$S_E = (1 - C)S_u \quad (7)$$

where  $S_E$  denotes the effective surface area of clay-coated detrital quartz and  $S_u$  denotes the specific surface area of uncoated quartz. Moreover, the model results indicate the significant dissolution of grain-coating clays (Section 3.1), which may lead to the partial or complete disappearance of clay coats and decreased coat coverage. However, a case study using natural sandstone samples rich in chlorite coats from a natural  $\text{CO}_2$  gas pool has illustrated an *in-situ* replacement process of chlorite coat by secondary calcite and kaolinite (Higgs et al., 2015), while secondary minerals retain grain-coating morphology. Therefore, in this study, a constant coat coverage was employed in a single simulation.

## 2.6 Water compositions

Subsurface pore water compositions are typically equilibrated with minerals at ambient conditions (Helgeson et al., 1993). On the basis of this conclusion, multiple reaction path models were conducted at different temperatures to derive water compositions. The initial water is consistently composed of 1.0 mol/kg NaCl solution. Moreover, the *in-situ* pH of sandstone formation water and shale produced water typically range from near neutral to mildly alkaline (Blondes et al., 2018). Therefore, the initial water pH was manually set to a value representing neutral pH at the respective temperatures. The initial mineralogy was arbitrarily set to be composed of 40% quartz, 30% K-feldspar, 10% clay, and 20% porosity. The resulting water compositions then served as the starting pore waters. Subsequently, different  $p\text{CO}_2$  values were introduced into the system, while pH was used to balance electric charge.

## 2.7 Mass transport kinetics

The mass transport process in all models is kinetically constrained using Fick's law (Fetter, 2014):

$$q = -\phi(a_L v + D_p) \frac{\partial C_f}{\partial d_f} \quad (8)$$

where  $q$  denotes the specific discharge rate,  $a_L$  denotes the horizontal dispersivity of the model domain,  $v$  denotes the averaged water flow speed,  $D_p$  denotes the coefficient of mass diffusion in the fluid,  $C_f$  denotes the species concentration in the fluid, and  $d_f$  denotes the flow distance. The term  $a_L$  is calculated by considering the empirical relationship with the horizontal domain length (Xu and Eckstein, 1995):

$$a_L = 0.83(\log L)^{2.414} \quad (9)$$

where  $L$  denotes the horizontal domain length. The term  $D_p$  can be calculated by (Schulz and Zabel, 2006):

$$D_p = \frac{D_f}{\theta^2} \quad (10)$$

where  $D_f$  denotes the coefficient of mass diffusion in free solutions and  $\theta$  denotes the tortuosity of the sediments.

The  $\theta$  can be calculated by Eq. (S1) considering the empirical relationship with sediment porosity. The  $D_f$  can be calculated by the following empirical regression relationship between the diffusion coefficient and temperature (Park, 2014):

$$D_f = (T_c + T_f T) \times 10^{-6} \quad (11)$$

where  $T_c$  and  $T_f$  are constants. The  $D_f$  values of available species were calculated (Table S2). As the GWB cannot separately input this parameter for each species, the averaged values of the calculated  $D_f$  at 60 °C ( $3.56 \times 10^{-5}$  cm<sup>2</sup>/s), 70 °C ( $3.98 \times 10^{-5}$  cm<sup>2</sup>/s), 80 °C ( $4.40 \times 10^{-5}$  cm<sup>2</sup>/s), 90 °C ( $4.83 \times 10^{-5}$  cm<sup>2</sup>/s), and 100 °C ( $5.25 \times 10^{-5}$  cm<sup>2</sup>/s) were considered (Table S2). The  $D_p$  was then calculated (Eq. (10)) based on the calculation of  $\theta$  considering variable coat volumes.

## 3. Results

In the following sections, model results from cases at 60 °C are mainly presented, as this temperature is typical for  $\text{CO}_2$  storage (Metz et al., 2005).

### 3.1 Geochemical reactions

The produced minerals using chlorite coats (Fig. 2(a)) are generally consistent with the results of the only experimental study involving clay coat dissolution (chamosite in this case) under  $\text{CO}_2$ -rich conditions (Luquot et al., 2012), as well as the diagenetic minerals observed in chamosite-coat-rich sandstones in a natural  $\text{CO}_2$  gas pool (Higgs et al., 2015). This validates the appropriate selection of secondary minerals in the models.

On the basis of the geochemical behaviours of clay coats, the four clay minerals could be classified into two categories: The chlorite coat, smectite coat, and illite coat exhibited different extents of dissolution behaviour (Figs. 2(a)-2(c)); while the kaolinite coat did not dissolve (Fig. 2(d)). Furthermore, the

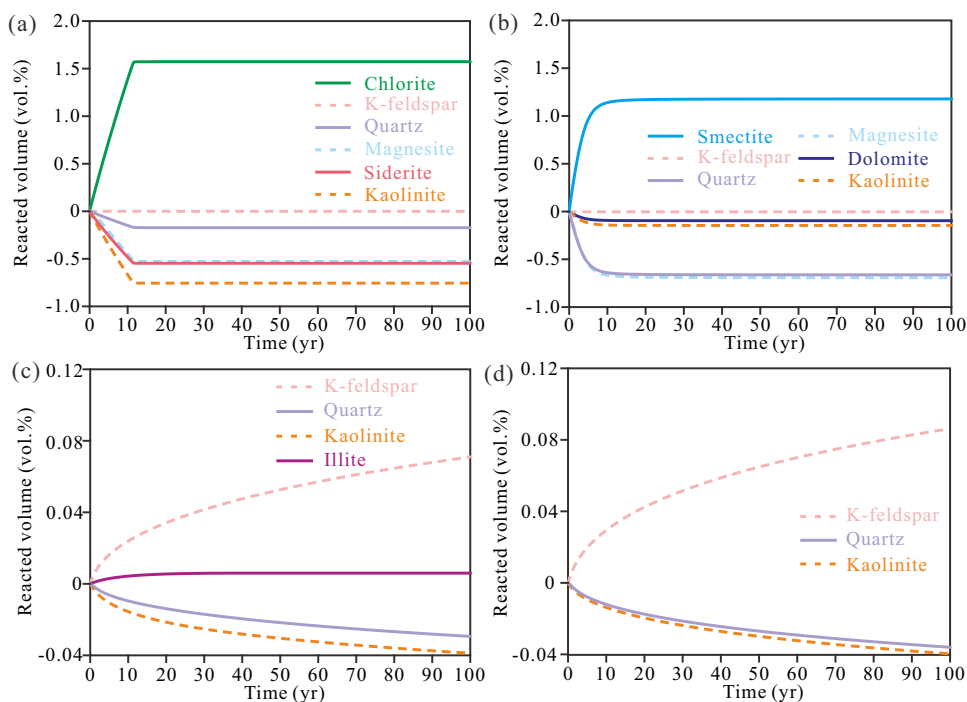


**Fig. 2.** Four examples illustrating mineral dissolution and precipitation using different grain-coating clay minerals at 60 °C. (a) Chlorite coat, (b) smectite coat, (c) illite coat and (d) kaolinite coat.  $p\text{CO}_2 = 10 \text{ MPa}$ ; coat thickness = 20  $\mu\text{m}$ ; coat coverage = 80%; grain size = 0.2 mm (fine sandstone).

dissolution amounts of chlorite and smectite were significantly greater than that of K-feldspar (Figs. 2(a)-2(b)), showing a dissolution priority of clay coats over detrital feldspar; however, the dissolution amount of illite was significantly lower than that of K-feldspar (Fig. 2(c)). Moreover, based on the products, the four clay minerals could also be classified into two categories: In illite-coated and kaolinite-coated sandstones, only quartz and kaolinite were precipitated (Figs. 2(c)-2(d)); while in chlorite-coated and smectite-coated sandstones, carbonate minerals (magnesite, siderite, and dolomite) were also precipitated (Figs. 2(a)-2(b)).

### 3.2 Water- $\text{CO}_2$ -rock interactions with variable clay coats

In the following sections, the model results from smectite coats are mainly presented. The results for different coat thicknesses, detrital grain sizes, detrital lithologies and the deceleration of K-feldspar dissolution rate are presented in the Supplementary Materials.

#### 3.2.1 Coat coverage

With the coat coverage increasing from 20% to 80%, pH gradually increased at the left domain, while it decreased at the right domain (Fig. 3(a)). However, a coat coverage of 100% exhibited the maximum decrease extent in pH. This unique characteristic mainly results from the complete inhibition of secondary quartz at a 100% coverage of clay coats (Fig. 3(b)). With the coat coverage increasing from 20% to 80%, the maximum  $\text{HCO}_3^-$  concentration increased, while the bicarbonation zone narrowed (Fig. 3(b)). In comparison,

a 100% coat coverage resulted in the maximum bicarbonation zone, whereas the maximum  $\text{HCO}_3^-$  concentration was smaller than those of 60% and 80% coat coverages (Fig. 3(b)). The  $\text{CO}_{2(\text{aq})}$  zone and  $\text{CO}_{2(\text{g})}$  zone narrowed with the coat coverage increasing from 20% to 80%, while a 100% coat coverage resulted in the maximum zones for both components (Figs. 3(c)-3(d)).

Regarding mineral dissolution, K-feldspar only extremely slightly dissolved (Fig. 3(f)). The smectite coat dissolved progressively more with the coat coverage increasing from 20% to 80%. A 100% coat coverage resulted in the maximum dissolution amount of smectite coat at the left end of domain albeit the minimum dissolution zone width (Fig. 3(e)). Regarding mineral precipitation, kaolinite, quartz, magnesite, and dolomite were increasingly precipitated with the coat coverage increasing from 20% to 80% (Figs. 3(g)-3(j)). As a result, the mineral carbonation amount increased. A 100% coat coverage led to the highest kaolinite precipitation at the left end of domain and the minimum dissolution zone width (Fig. 3(g)). In comparison, it resulted in no quartz precipitation (Fig. 3(h)), the lowest precipitation of dolomite and magnesite (Figs. 3(i)-3(j)), and the minimum mineral carbonation amount (Fig. 3(k)). With the coverage of clay coats increasing from 20% to 80%, porosity significantly decreased, while a 100% coat coverage resulted in porosity increase alone within the entire domain (Fig. 3(l)).

For a coat coverage ranging from 20% to 80%, the differences in the examined parameters between the grain-coating and pore-filling scenarios were relatively minor. In comparison, for a 100% coat coverage, the grain-coating

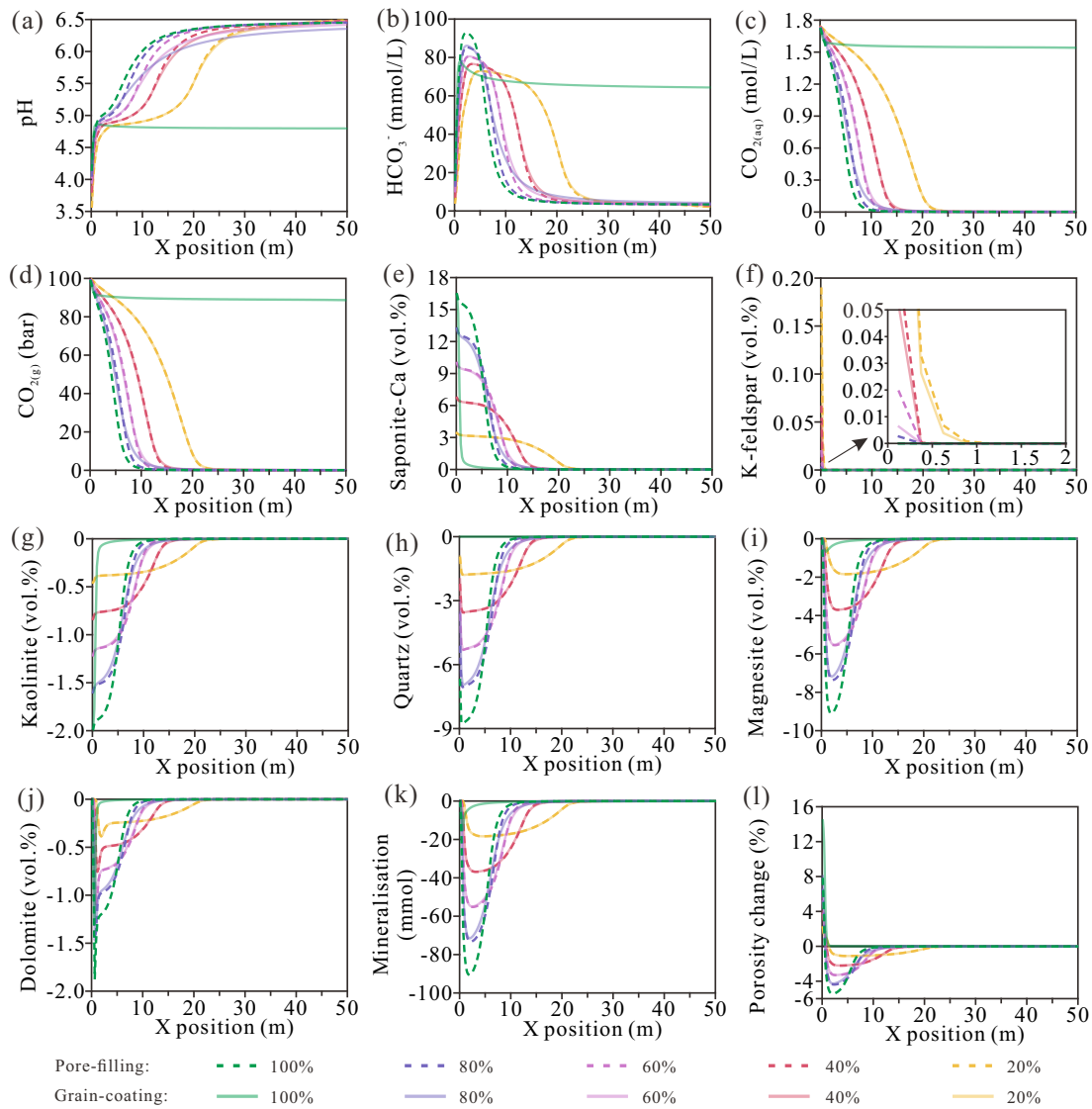


**Fig. 3.** Changes in (a) water pH, (b)-(d)  $\text{CO}_2$  speciation, (e)-(j) mineral dissolution and precipitation, (k) mineral trapping of  $\text{CO}_2$  and (l) porosity changes using different coat coverages over 100 years.  $p\text{CO}_2 = 10$  MPa; velocity = 0.1 m/yr; coat thickness = 20  $\mu\text{m}$ ; grain size = 0.2 mm (fine sandstone).

scenario resulted in significantly lower pH (Fig. 3(a)), significantly lower  $\text{HCO}_3^-$  concentrations at the left domain and higher  $\text{HCO}_3^-$  concentrations at the right domain (Fig. 3(b)), significantly higher  $\text{CO}_{2(\text{aq})}$  and  $\text{CO}_{2(\text{g})}$  (Figs. 3(b)-3(d)), significantly lower dissolution volume of smectite coat (Fig. 3(e)), significantly lower precipitation volumes of kaolinite, quartz, magnesite, and dolomite (Figs. 3(g)-3(j)), significantly lower mineral carbonation amount (Fig. 3(k)), and porosity decrease (Figs. 3(l)).

### 3.2.2 Clay mineralogy

Different grain-coating clay minerals result in significant differences in the examined parameters, as illustrated in Fig. 4. The utilized four grain-coating clays could be classified into two groups: Both chlorite and smectite resulted in the precipitation of carbonates (Fig. 4(i)), while both kaolinite and illite did not. In general, chlorite coat resulted in the

highest pH, followed by smectite, illite and kaolinite (Fig. 4(a)). Both chlorite and smectite resulted in higher  $\text{HCO}_3^-$ ,  $\text{CO}_{2(\text{aq})}$ , and  $\text{CO}_{2(\text{g})}$  at the left model domain compared to the middle and right model domains (Figs. 4(b)-4(d)). In comparison, both illite and kaolinite resulted in lower  $\text{HCO}_3^-$  and higher  $\text{CO}_{2(\text{aq})}$  and  $\text{CO}_{2(\text{g})}$  at the left domain compared to the right domain (Figs. 4(b)-4(d)). Both chlorite and smectite exhibited significant dissolution behaviours (Fig. 4(e)). In comparison, illite exhibited only minor dissolution behaviour, while kaolinite exhibited only precipitation behaviour (Fig. 4(e)). Both chlorite and smectite resulted in no identifiable dissolution of K-feldspar, while both illite and kaolinite resulted in significant K-feldspar dissolution (Fig. 4(f)). Both chlorite and smectite coats resulted in significantly higher kaolinite precipitation compared to illite and kaolinite coats (Fig. 4(g)). Since the coat coverages for four clay coats were consistently 100%, there is consistently no quartz precipitation for the

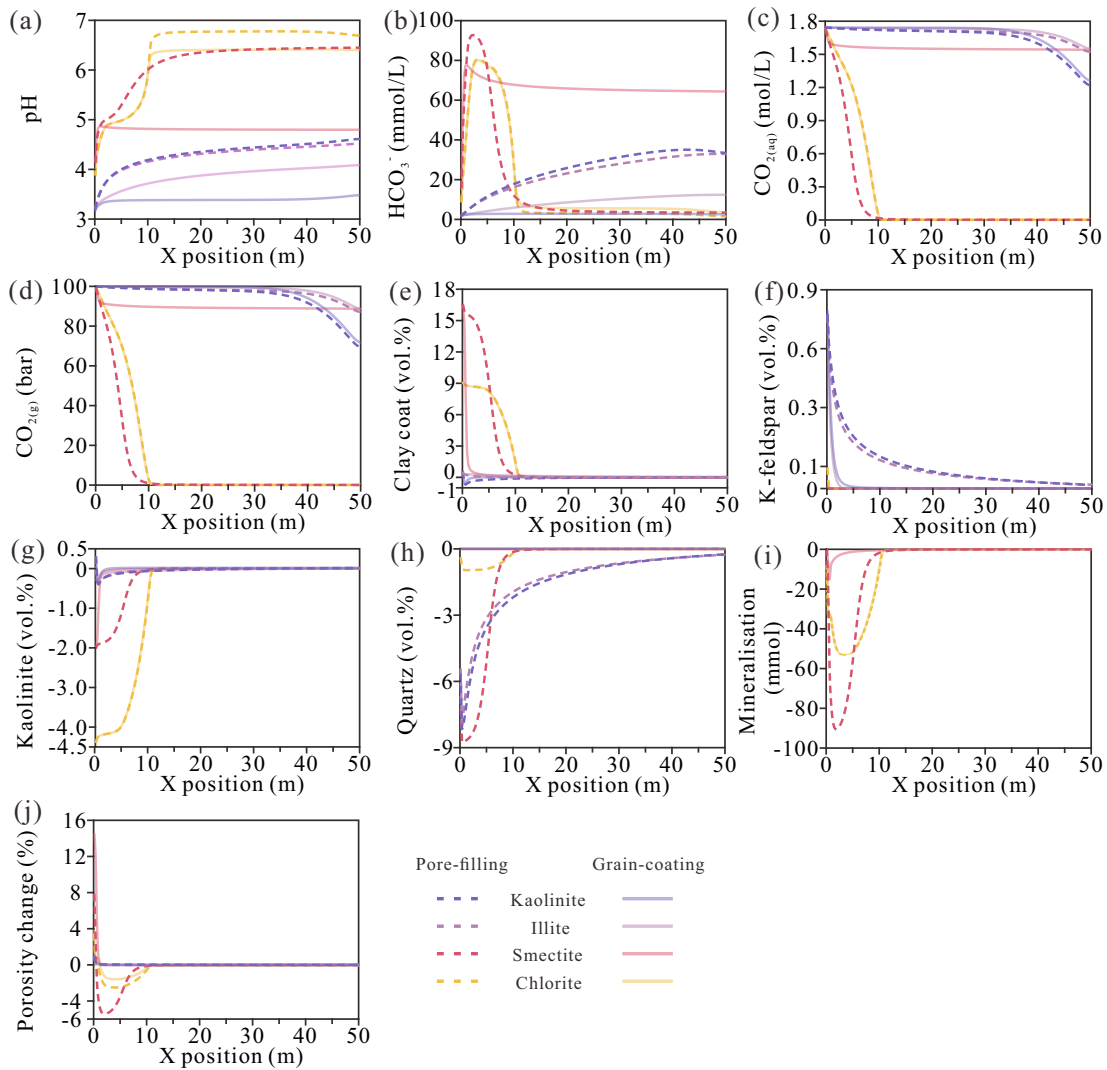


**Fig. 4.** Changes in (a) water pH, (b)-(d) CO<sub>2</sub> speciation, (e)-(h) mineral dissolution and precipitation, (i) mineral trapping of CO<sub>2</sub> and (j) porosity changes using different grain-coating clay mineralogy over 100 years.  $p\text{CO}_2 = 10$  MPa; velocity = 0.1 m/yr; coat thickness = 20  $\mu\text{m}$ ; grain size = 0.2 mm (fine sandstone).

four clay coats (Fig. 4(h)). Smectite, illite and kaolinite coats consistently resulted in no porosity decrease, while only the chlorite coat resulted in a porosity decrease (Fig. 4(j)).

The pore-filling scenarios of four clay coats consistently resulted in significantly higher quartz precipitation compared to the grain-coating scenario (Fig. 4(h)). For the chlorite coat, the pore-filling scenario led to significantly higher pH (Fig. 4(a)) and porosity change (Fig. 4(j)) compared to the grain-coating scenario, while there were no identifiable differences in CO<sub>2</sub> speciation (Figs. 4(b)-4(d)), the dissolution volumes of chlorite and K-feldspar (Figs. 4(e)-4(f)), kaolinite precipitation (Fig. 4(g)), and mineral carbonation (Fig. 4(i)) between these two scenarios. For smectite, illite, and kaolinite coats, the pore-filling scenarios resulted in significantly higher pH compared to the grain-coating scenario (Fig. 4(a)). The pore-filling scenarios of both illite and kaolinite coats resulted in significantly higher HCO<sub>3</sub><sup>-</sup> concentration compared to the grain-coating scenario (Fig. 4(b)), while the pore-filling scenario of smectite coat generally resulted in a significantly higher HCO<sub>3</sub><sup>-</sup> con-

centration at the left domain compared to the grain-coating scenario and a significantly lower HCO<sub>3</sub><sup>-</sup> concentration at the right domain (Fig. 4(b)). The pore-filling scenarios of illite and kaolinite coats resulted in slightly lower CO<sub>2(aq)</sub> and CO<sub>2(g)</sub> compared to the grain-coating scenario, while the pore-filling scenario of smectite coat resulted in significantly lower CO<sub>2(aq)</sub> and CO<sub>2(g)</sub> (Figs. 4(c)-4(d)). Moreover, the pore-filling scenarios of illite and kaolinite coats resulted in minor differences in clay coat dissolution or precipitation (Fig. 4(e)), kaolinite precipitation (Fig. 4(g)), and porosity change (Fig. 4(j)), while they resulted in significantly higher K-feldspar dissolution (Fig. 4(f)). In comparison, the pore-filling scenario of smectite coat resulted in significantly higher smectite dissolution (Fig. 4(e)), no identifiable differences in K-feldspar dissolution (Fig. 4(f)), and significantly higher precipitation of kaolinite (Fig. 4(g)), mineral carbonation (Fig. 4(i)), and porosity decrease (Fig. 4(j)).

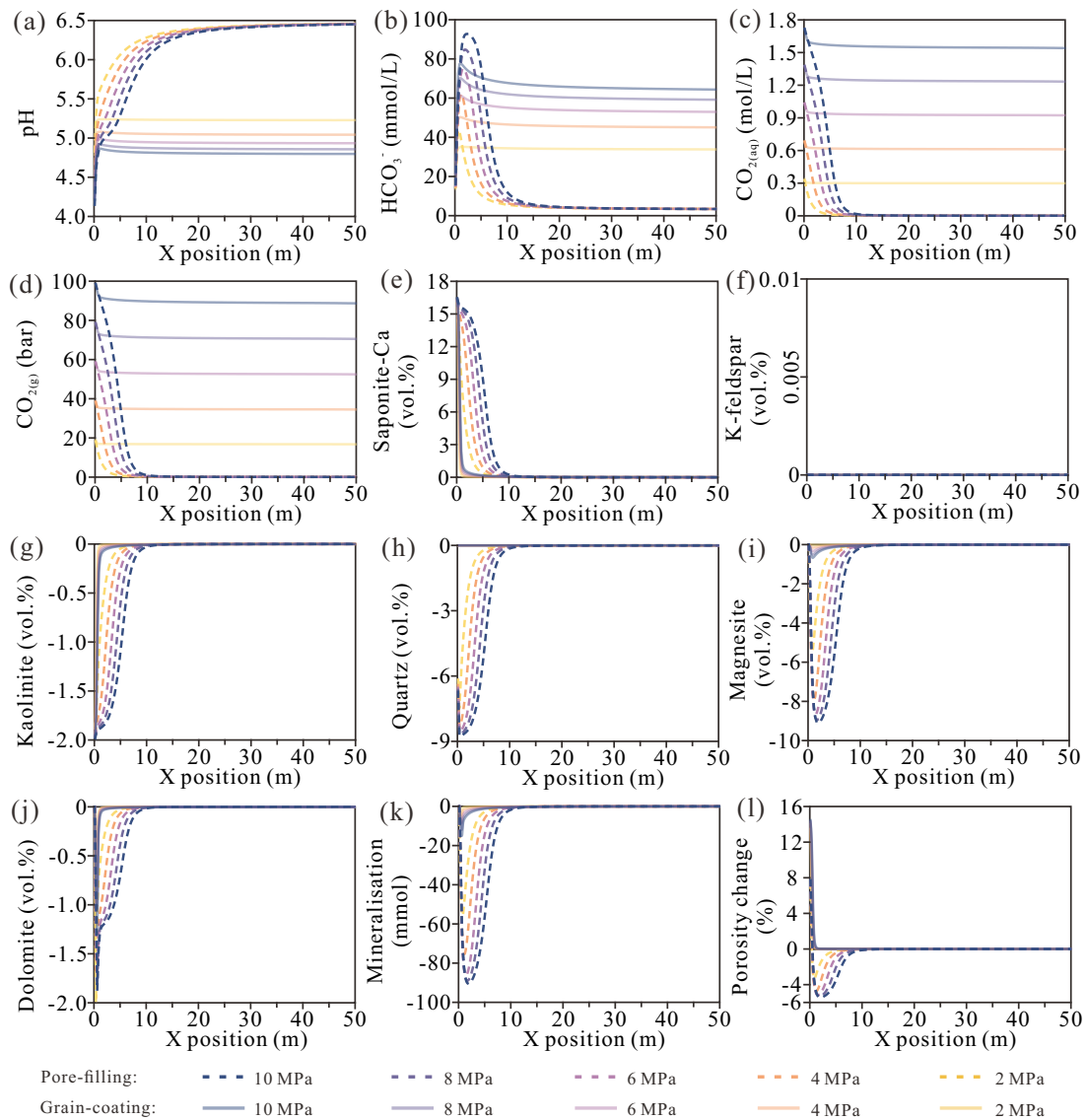


**Fig. 5.** Changes in (a) water pH, (b)-(d) CO<sub>2</sub> speciation, (e)-(j) mineral dissolution and precipitation, (k) mineral trapping of CO<sub>2</sub> and (l) porosity changes using different  $p\text{CO}_2$  over 100 years. Velocity = 0.1 m/yr; coat thickness = 20  $\mu\text{m}$ ; coat volume = 12.38%; grain size = 0.2 mm (fine sandstone).

### 3.3 Water-CO<sub>2</sub>-rock interactions with variable $p\text{CO}_2$

Increasing the  $p\text{CO}_2$  from 2 to 10 MPa resulted in significantly decreased pH (Fig. 5(a)), significantly increased  $\text{HCO}_3^-$ ,  $\text{CO}_{2(\text{aq})}$ , and  $\text{CO}_{2(\text{g})}$  (Figs. 5(b)-5(d)), slightly increased smectite dissolution (Fig. 5(e)), no identifiable difference in K-feldspar dissolution and quartz precipitation (Figs. 5(f) and 5(h)), slightly increased precipitation of kaolinite, magnesite and dolomite (Figs. 5(g), 5(i), and 5(j)), and slightly increased mineral carbonation and porosity increase (Figs. 5(k)-5(l)). The pore-filling scenarios resulted in significant differences in the examined parameters compared to the grain-coating scenarios (Fig. 5), which is analogous to the results of 100% coat coverage as described in Section 3.2.1.

### 3.4 Water-CO<sub>2</sub>-rock interactions at variable temperatures

Increasing the temperature from 60 to 100 °C led to only very minor changes in pH (Fig. 6(a)),  $\text{CO}_{2(\text{g})}$  (Fig. 6(d)), the dissolution of primary minerals, the precipitation of secondary minerals (Figs. 6(e)-6(j)), mineral carbonation (Fig. 6(k)), and porosity change (Fig. 6(l)). For example, the maximum mineral carbonation ranged from 10.87 (100 °C) to 15.1 mmol (60 °C); the porosity increase ranged from 14.45% (60 °C) to 15.11% (100 °C). In comparison, increasing temperature led to significantly reduced  $\text{HCO}_3^-$  and  $\text{CO}_{2(\text{aq})}$  (Figs. 6(b)-6(c)). The pore-filling scenarios resulted in significant differences in the examined parameters compared to the grain-coating scenarios (Fig. 6), which is analogous to the results of 100% coat coverage as described in Section 3.2.1.



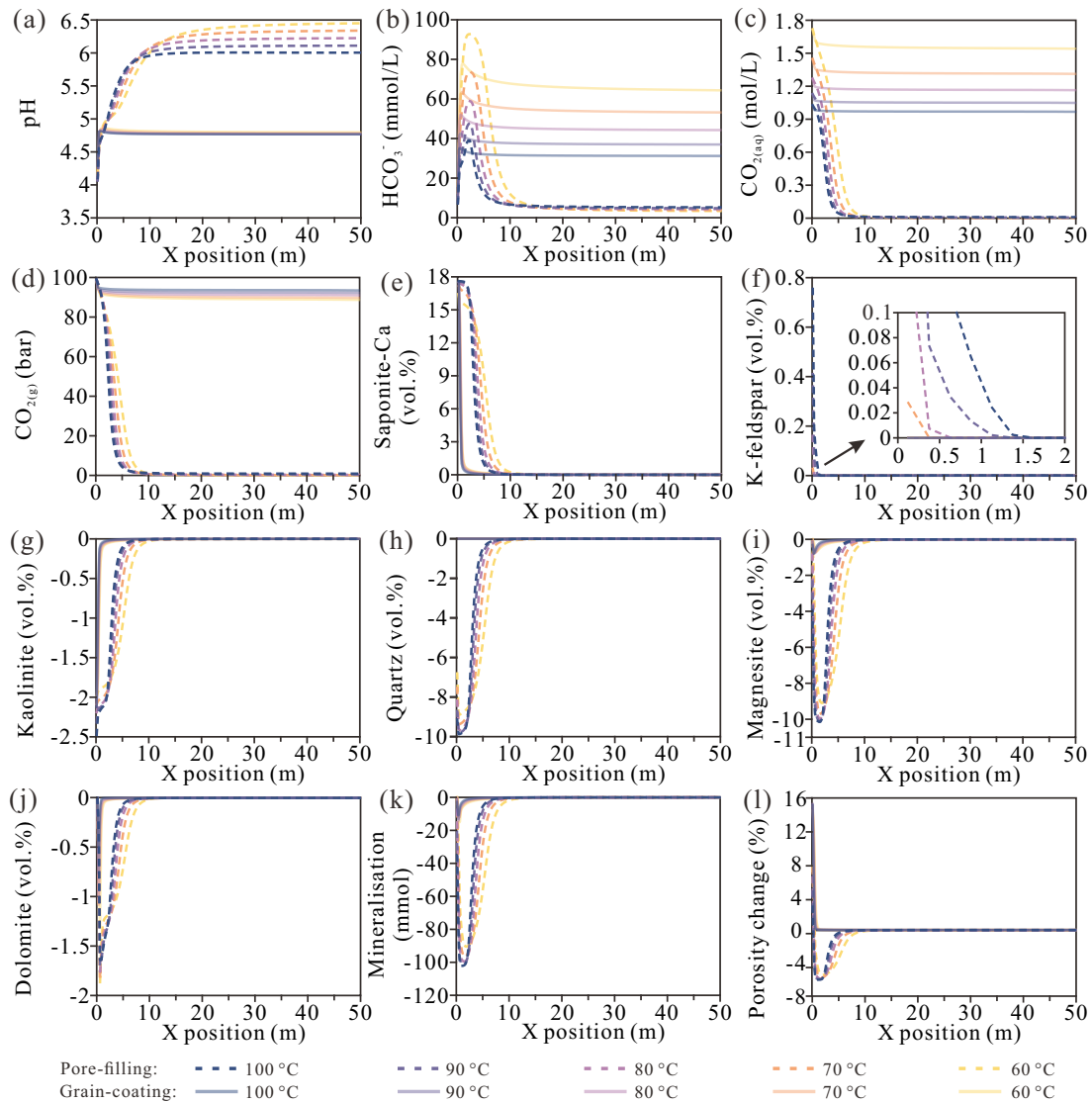


**Fig. 6.** Changes in (a) water pH, (b)-(d)  $\text{CO}_2$  speciation, (e)-(j) mineral dissolution and precipitation, (k) mineral trapping of  $\text{CO}_2$  and (l) porosity changes using different temperatures over 100 years.  $p\text{CO}_2 = 10$  MPa; velocity = 0.1 m/yr; coat thickness = 20  $\mu\text{m}$ ; coat volume = 12.38%; grain size = 0.2 mm (fine sandstone).

### 3.5 Water- $\text{CO}_2$ -rock interactions with variable fluid velocities

Increasing the fluid velocity resulted in significantly decreased pH and  $\text{HCO}_3^-$  at the left domain, and slightly increased pH and significantly increased  $\text{HCO}_3^-$  at the right domain (Figs. 7(a)-7(b)). With increasing fluid velocity,  $\text{CO}_{2(\text{aq})}$ ,  $\text{CO}_{2(\text{g})}$ , and the dissolution of smectite and K-feldspar were significantly increased (Figs. 7(c)-7(f)). Kaolinite was also generally significantly increased (Fig. 7(g)). Meanwhile, magnesite, dolomite, and mineral carbonation exhibited single-peak distributions and the X-positions of the peaks shifted from left to right of the domain (Figs. 7(i)-7(k)), indicating the re-dissolution of secondary carbonates. The maximum mineral carbonation decreased from 34.01 (0.1 m/yr) to 15.10 mmol (10 m/yr). Additionally, the porosity increase was significant (Fig. 7(l)), with the maximum porosity increase rising from

14.44% (0.1 m/yr) to 18.45% (10 m/yr).

For different fluid velocities, the pore-filling scenario resulted in diverse differences in the examined parameters compared to the grain-coating scenario. Regarding pH, the fluid flow rates of 0.1 and 1 m/yr of pore-filling scenarios resulted in pH decrease at the left domain but pH increase at the right domain (Fig. 7(a)); in comparison, a velocity of 10 m/yr of pore-filling scenario resulted in pH decrease at the entire domain (Fig. 7(a)). Regarding  $\text{HCO}_3^-$ , a velocity of 0.1 m/yr of pore-filling scenario resulted in  $\text{HCO}_3^-$  increase at the left domain and decrease at the right domain (Fig. 7(b)); a velocity of 1 m/yr of pore-filling scenario resulted in  $\text{HCO}_3^-$  decrease at the left domain and increase at the right domain (Fig. 7(b)); meanwhile, a velocity of 10 m/yr of pore-filling scenario resulted in  $\text{HCO}_3^-$  decrease at the entire domain (Fig. 7(b)). Regarding  $\text{CO}_{2(\text{aq})}$  and  $\text{CO}_{2(\text{g})}$ , a velocity of 0.1 m/yr of pore-filling scenario resulted in a decrease in both

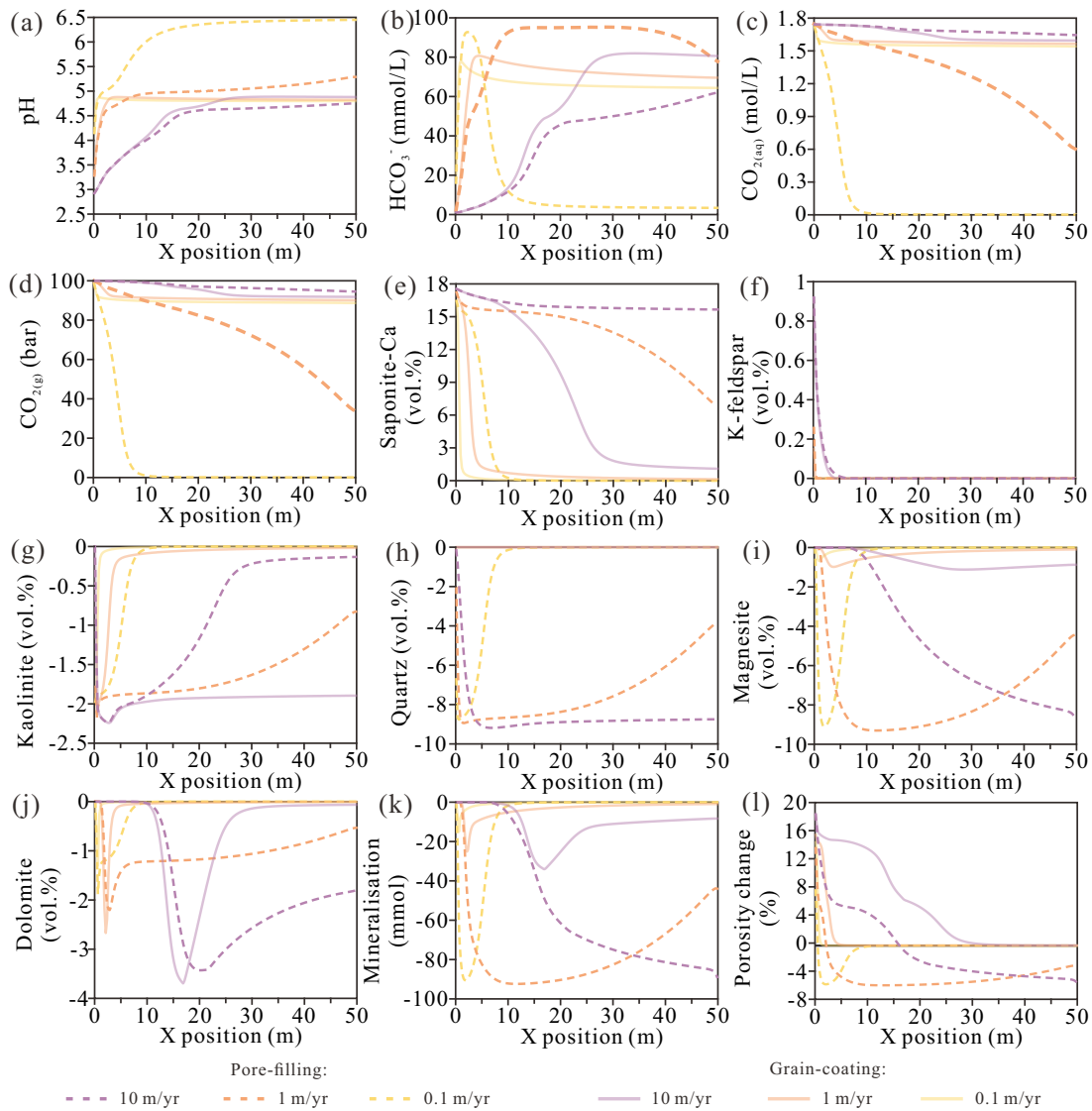


**Fig. 7.** Changes in (a) water pH, (b)-(d) CO<sub>2</sub> speciation, (e)-(j) mineral dissolution and precipitation, (k) mineral trapping of CO<sub>2</sub> and (l) porosity changes using different fluid flow rates over 100 years.  $p\text{CO}_2 = 10 \text{ MPa}$ ; coat thickness = 20  $\mu\text{m}$ ; coat volume = 12.38%; grain size = 0.2 mm (fine sandstone).

parameters at the entire domain (Figs. 7(c)-7(d)); a velocity of 1 m/yr of pore-filling scenario resulted in an increase in both parameters at the right domain but a decrease in both parameters at the right domain (Figs. 7(c)-7(d)); a velocity of 10 m/yr of pore-filling scenario resulted in an increase in both parameters throughout the entire domain (Figs. 7(c)-7(d)).

Moreover, the pore-filling scenarios consistently resulted in an increased dissolution of smectite and K-feldspar (Figs. 7(e)-7(f)). Kaolinite precipitation was significantly increased for the pore-filling scenarios using velocities of 0.1 and 1 m/yr (Fig. 7(g)). In comparison, a velocity of 10 m/yr led to significantly decreased kaolinite precipitation (Fig. 7(g)). The pore-filling scenarios consistently resulted in significantly increased quartz precipitation (Fig. 7(h)). Regarding carbonates, the pore-filling scenarios consistently resulted in significantly increased precipitation of carbonates and mineral carbonation amount (Figs. 7(i)-7(k)). Furthermore, compared to the grain-

coating scenarios, the X-positions of the peaks for the pore-filling scenarios slightly shifted from left to right of the domain (Figs. 7(i)-7(k)). Regarding porosity change, the pore-filling scenarios consistently resulted in a porosity decrease, while only porosity increases were observed for the grain-coating scenarios (Fig. 7(l)).

## 4. Discussion

### 4.1 Impacts of clay coats on geochemical reactions

#### 4.1.1 Comparison between grain-coating and pore-filling clays

The two differences in model settings between the pore-filling scenario and the grain-coating scenario are that both the detrital quartz surface area and the dissolution rate of K-feldspar were decreased in the grain-coating scenario. Based

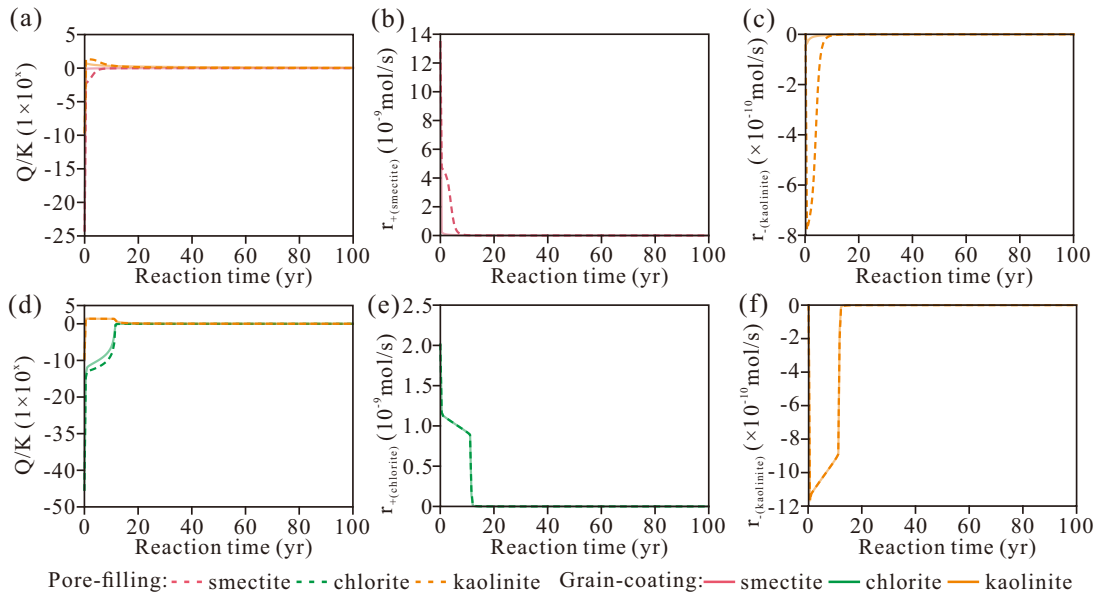
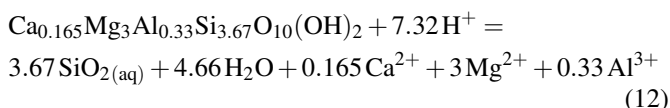


**Fig. 8.** (a) and (d) Saturation index ( $Q/K$ ) of clay coats and kaolinite, (b) and (e) dissolution rate of clay coats ( $r_+$ ), and (c) and (f) precipitation rate of kaolinite ( $r_-$ ) in smectite-coated and chlorite-coated sandstones over 100 years.  $p\text{CO}_2 = 10$  MPa; coat thickness = 4  $\mu\text{m}$ ; grain size = 0.2 mm (fine sandstone).

on the relative importance of these two factors, the four involved clay coats could be classified into two categories. For the first category, K-feldspar was only extremely slightly dissolved in both chlorite-coated and smectite-coated sandstones (Figs. 2 and 4(f)), which indicates a selective dissolution of chlorite and smectite coats over detrital K-feldspar. The deceleration of K-feldspar dissolution rate only plays a minor role in causing the difference between the grain-coating and pore-filling scenarios (Fig. S4). In this way, the inhibition of secondary quartz is the main mechanism causing the difference between the grain-coating and pore-filling scenarios for the chlorite and smectite coats. For the second category, K-feldspar was significantly dissolved for both illite-coated and kaolinite-coated sandstones (Figs. 2 and 4(f)). The deceleration of K-feldspar dissolution rate can lead to remarkable changes in the examined geochemical parameters (Figs. S20 and S28). In this way, the difference between the grain-coating and pore-filling scenarios for the illite coat and the kaolinite coat should be ascribed to both the inhibition of secondary quartz and the deceleration of K-feldspar dissolution rate due to clay coats.

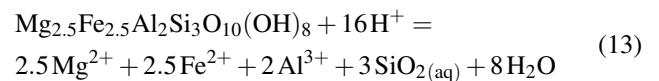
For the first category, taking smectite coat as an example, with a smectite coat coverage of 100%, the pore-filling scenarios consistently resulted in significant changes in the examined parameters (Figs. 5-7). Moreover, Fig. 2(b) illustrates that the main  $\text{SiO}_{2(\text{aq})}$  source for secondary quartz is smectite dissolution, while K-feldspar is only extremely slightly dissolved. Smectite takes the following reaction path to produce  $\text{SiO}_{2(\text{aq})}$  (Bethke, 2008):



The inhibition of secondary quartz could significantly

increase the concentration of dissolved  $\text{SiO}_{2(\text{aq})}$  and increase the saturation index of smectite with respect to pore water (Fig. 8(a)). Smectite dissolution was significantly reduced for the grain-coating scenario compared to the pore-filling scenario (Fig. 8(b)). As a result, the dissolution amount of smectite coat was significantly reduced in the grain-coating scenario compared to the pore-filling scenario (e.g., Fig. 5(e)). Since smectite was the only dissolved mineral, the products of smectite dissolution, including kaolinite, magnesite, and dolomite, were consistently reduced compared to the pore-filling scenarios (e.g., Figs. 5(g), 5(i), and 5(j)).

Regarding the chlorite coat, although secondary quartz was also significantly inhibited in the grain-coating scenario, there were no identifiable differences in the geochemical reactions of other minerals (Figs. 4(e)-4(g) and 4(i); Figs. 8(e)-8(f)). This is contradictory to the conclusions from smectite coat. Chlorite takes the following reaction for dissolution (Bethke, 2008):



It is important to note that although chlorite is also the main  $\text{SiO}_{2(\text{aq})}$  source for secondary quartz in chlorite-coated sandstones,  $\text{SiO}_{2(\text{aq})}$  sinks include quartz and kaolinite. In the dissolution reaction of smectite (Eq. (12)), the produced  $\text{SiO}_{2(\text{aq})}$  amount was  $\sim 11.1$  times higher than  $\text{Al}^{3+}$ . In comparison, in the dissolution reaction of chlorite (Eq. (13)), the produced  $\text{SiO}_{2(\text{aq})}$  amount was only 1.5 times higher than  $\text{Al}^{3+}$ . The molar ratio of Al:Si in kaolinite was 1. Regarding smectite dissolution, a single precipitation dissolved of kaolinite only consumes one unit of  $\text{SiO}_{2(\text{aq})}$ , leaving 10.1 units of  $\text{SiO}_{2(\text{aq})}$  in the aqueous phase. In comparison, regarding chlorite dissolution, a single precipitation unit of kaolinite leaves only 0.5 unit of  $\text{SiO}_{2(\text{aq})}$  in the aqueous phase. In this

way, the inhibition of secondary quartz (a sink for  $\text{SiO}_2$ ) could significantly impact the smectite dissolution rate (Fig. 8(b)) and the kaolinite precipitation rate (Fig. 8(c)), while it only had minor influences on the chlorite dissolution rate (Fig. 8(e)) and the kaolinite precipitation rate (Fig. 8(f)).

For the second category, taking kaolinite coat as an example, the increased K-feldspar dissolution rate deceleration resulted in significantly reduced K-feldspar dissolution for both the grain-coating and pore-filling scenarios (Fig. S20(e)). Furthermore, the difference in the examined parameters between the grain-coating and pore-filling scenarios became smaller with a higher K-feldspar dissolution rate deceleration. For example, at an X position = 5 m, the K-feldspar dissolution amount for pore-filling scenario without K-feldspar dissolution rate reduction was  $\sim 30$  times higher than that in the grain-coating scenario (Fig. S20(e)). With  $10^{-3}$  K-feldspar dissolution rate deceleration, the K-feldspar dissolution amount in the pore-filling scenario was  $\sim 0.9$  times that in the grain-coating scenario. In other words, if K-feldspar dissolution rate deceleration is taken into consideration, it may weaken the inhibitory effect of clay coats on quartz cements.

#### 4.1.2 Factors impacting the role of clay coats

The role of grain-coating clays is controlled by multiple elements simultaneously. The attributes of grain-coating clays, fluid flow velocity and detrital grain size exhibited strong influences on all the examined geochemical parameters (Figs. 3, 4, 7, and S2). The attributes of clay coats and detrital grain size mainly control the volume of clay coat (Eq. (1)). A higher coverage and thickness of clay coats as well as a smaller grain size leads to a higher clay coat volume and a higher bulk clay surface area, ultimately generating a higher clay dissolution rate (Eq. (2)). In this way, a higher coverage and thickness of clay coats as well as a smaller grain size could lead to the increased dissolution of clay coats (Figs. 3(e), 5(e), and S2(e)). At the same time, coat coverage also controls the inhibition of quartz cements. A higher coat coverage resulted in an increased inhibition of quartz cements (Fig. 3(h)). A higher velocity brings more acidic  $\text{CO}_2$ -rich fluid passing through the model domain, which leads to a pH decrease (Fig. 7(a)) and increased mineral dissolution (Figs. 7(e)-7(f)).

Neither sandstone lithology nor K-feldspar dissolution rate deceleration had an identifiable influence on all the examined geochemical parameters (Figs. S3 and S4). The same conclusions can be drawn for chlorite coats (Figs. S8 and S12). This can be explained by the prioritized dissolution of smectite and chlorite over K-feldspar (Figs. 2(a)-2(b), S3(e)-S3(f), and S4(e)-S4(f)). In comparison, for the illite and kaolinite coats, variations in detrital sandstone lithology and K-feldspar dissolution rate deceleration can lead to noticeable changes in the examined geochemical parameters (Figs. S16, S20, S24, and S28). This can be explained by the prioritized dissolution of K-feldspar over illite and kaolinite (Figs. 2(c)-2(d)).

Although  $p\text{CO}_2$  could significantly impact pH and  $\text{CO}_2$  speciation for smectite-coated sandstones (Fig. 5), it had only very minor influences on the other examined geochemical parameters (Figs. 5(e)-5(l)). The same conclusions can be drawn for kaolinite-coated sandstones (Fig. S17). In comparison, for

the illite coat,  $p\text{CO}_2$  could also significantly impact illite dissolution and kaolinite precipitation in addition to pH and  $\text{CO}_2$  speciation (Fig. S25). For the chlorite coat,  $p\text{CO}_2$  could significantly impact all the examined parameters (Fig. S9).

Temperature could only significantly impact  $\text{HCO}_3^-$  and  $\text{CO}_2(\text{aq})$  concentrations, while it only had minor influences on the other parameters (Fig. 6). The same conclusions can be drawn for kaolinite-coated sandstones (Fig. S18). In comparison, for chlorite coats, temperature could impact all the examined parameters (Fig. S10). For the illite coat, temperature could also significantly impact illite dissolution in addition to pH and  $\text{CO}_2(\text{aq})$  (Fig. S26).

#### 4.2 Implications for $\text{CO}_2$ storage

This work evaluated the residual trapping, solubility trapping, and mineral trapping mechanisms, while structural trapping was not evaluated because the sandstone formation structures were not considered.

Secondary carbonates were only precipitated in smectite-coated and chlorite-coated sandstones, while there was no carbonate precipitation in kaolinite-coated and illite-coated sandstones (Figs. 2 and 4(i)). Therefore, only residual trapping and solubility trapping are important for the kaolinite and illite coats. Notably,  $\text{CO}_2$  trapped by secondary carbonates in the smectite coat was significantly lower than that in the chlorite coat (Fig. 4(i)). Grain-coating smectite resulted in significantly lower mineral carbonation than pore-filling smectite (Fig. 4(i)). In comparison, there were no identifiable differences in mineral carbonation between grain-coating and pore-filling chlorite (Fig. 4(i)). It is important to note that the predominant forms of injecting  $\text{CO}_2$  were gaseous and aqueous  $\text{CO}_2$ , followed by  $\text{HCO}_3^-$ , for all clays (Figs. 4(b)-4(d)).

The reaction fronts for smectite coat and chlorite coat with an initial fluid velocity of 0.1 m/yr over 100 years were located at the X position of 10-15 m (e.g., Fig. 4(b)). However, the reaction fronts for kaolinite coat and illite coat traversed the entire model domain (e.g., Fig. 4(b)). This may indicate that the transport rates of injecting  $\text{CO}_2$  in smectite-coated and chlorite-coated sandstones would be significantly lower than those in kaolinite-coated and illite-coated sandstones under the same injecting pressure.

The porosity decrease after the injection of  $\text{CO}_2$  was only observed for chlorite-coated sandstones (Fig. 4(j)), while the porosity was only increased for the other three clay coats. Therefore, the  $\text{CO}_2$  storage capacity in chlorite-coated sandstones may be decreased. This seems contradictory to the flow-through dissolution results using chamosite-coat-rich sandstones under  $\text{CO}_2$ -rich conditions (Luquot et al. (2012)), in which a porosity increase was observed. However, the reactor size in Luquot et al. (2012)'s study was only 18 mm. It should be noted that porosity was increased at the left end of model domain (Fig. 4(j)). Therefore, the experimental results of Luquot et al. (2012) are more analogous to our model results close to the left model end.

### 4.3 Uncertainties

It is important to note that the uncertainties associated with the reactive transport model settings may cause discrepancies in the results and conclusions derived from numerical models. Typically, the accessible surface area and mineral dissolution-precipitation kinetics represent two major gaps constraining model precision. Under CO<sub>2</sub>-rich conditions (HCO<sub>3</sub><sup>-</sup>-buffered system), the adsorption of HCO<sub>3</sub><sup>-</sup> may inhibit the mineral dissolution rate (Black and Haese, 2014). The HCO<sub>3</sub><sup>-</sup> concentration in our models lied at  $\sim 5 - 95 \times 10^{-3}$  mol/L (Figs. 3-7). However, chlorite powder dissolution experiments under 50~120 °C and *p*CO<sub>2</sub> of 120 ~ 200 bar (Black and Haese, 2014) have indicated that increasing HCO<sub>3</sub><sup>-</sup> concentrations in this range at 50 ~ 120 °C may reduce chlorite dissolution rate by no more than half an order of magnitude. Moreover, alkali feldspar dissolution experiments under 22 ~ 200 °C and *p*CO<sub>2</sub> of 0.3 ~ 20 MPa also suggested that the dissolution rate is comparable to those in other acidic conditions (Rosenqvist et al., 2019). Nevertheless, it is still recommended to consistently employ mineral dissolution kinetics measured in CO<sub>2</sub>-rich experiments.

Moreover, although this study revealed a decrease in detrital quartz surface area and K-feldspar dissolution rate by clay coats, the quantitative mechanisms remain unclear. Additionally, clay minerals typically have large specific surface areas, potentially leading to the significant adsorption of gas and aqueous species onto the clay surface, which mechanism is not considered in the current models. Future studies may be dedicated to tackling these gaps and challenges to potentially improve model precision.

### 5. Conclusions and remarks

In this work, the impacts of clay coats on geochemical reactions in sandstones involving CO<sub>2</sub> have been illustrated. In essence, grain-coating clays exert influences on water-CO<sub>2</sub>-rock interactions mainly through three mechanisms, including inhibiting secondary quartz precipitation, reducing the detrital K-feldspar dissolution rate and the dissolution of clay coats. Grain-coating clays, compared to pore-filling clays, can lead to significant differences in water pH, CO<sub>2</sub> speciation, the dissolution of primary minerals, the precipitation of secondary minerals, and porosity change. Moreover, several parameters may impact the role of clay coats, including clay coat attributes, detrital grain size, detrital lithology, *p*CO<sub>2</sub>, temperature, and fluid flow velocity.

Mineral carbonation only occurs in the smectite coat chlorite coats, while porosity decrease only occurs for the chlorite coat. This may also lead to permeability decrease, as permeability (*K*) is usually positively correlated with porosity: In this case,  $\log K = 15\phi - 5$  (Bethke, 2008). This is consistent with the experimental study using chamosite-coat-rich sandstones under CO<sub>2</sub>-rich conditions (Luquot et al., 2012). According to Darcy's law,  $q = K\Delta p/\Delta L$ , where *p* stands for pressure difference. The permeability reduction of a porous medium requires an increased pressure drop to maintain a constant discharge. This may indicate that a higher injection pressure is required in chlorite-coated sandstones to promote

CO<sub>2</sub> injection efficiency. The abundance of chlorite coats in natural sandstones has been suggested to be higher in deltaic systems (Worden et al., 2020; Akinlotan et al., 2024). To avoid potential porosity/permeability decrease, such environments may not be considered with priority for CO<sub>2</sub> storage.

### Acknowledgements

This study was financially supported by the Hubei Provincial 100-Talent Program 2025, the National Postdoctoral Researchers Program (No. GZC20250293) and the China Postdoctoral Science Foundation (No. 2025M770446). Gratitude is given to Dr. Robert Lander (Geocosm LLC, USA) for initially suggesting us to conduct this research.

### Supplementary file

<https://doi.org/10.46690/ager.2025.08.04>

### Conflict of interest

The authors declare no competing interest.

**Open Access** This article is distributed under the terms and conditions of the Creative Commons Attribution (CC BY-NC-ND) license, which permits unrestricted use, distribution, and reproduction in any medium, provided the original work is properly cited.

### References

- Akinlotan, O. O., Moghalu, O. A., Hatter, S. J., et al. Paleoclimatic controls on clay mineral distribution in the Early Cretaceous (Barremian): The Wessex Basin, Southeast England. *Journal of Earth Science*, 2024, 35, 2050-2066.
- Alansari, A., Salim, A. M. A., Janjuhah, H. T., et al. Quantification of clay mineral microporosity and its application to water saturation and effective porosity estimation: A case study from Upper Ordovician reservoir, Libya. *Journal of Natural Gas Geoscience*, 2019, 4(3): 139-150.
- Beckingham, L. E., Mitnick, E. H., Steefel, C. I., et al. Evaluation of mineral reactive surface area estimates for prediction of reactivity of a multi-mineral sediment. *Geochimica et Cosmochimica Acta*, 2016, 188: 310-329.
- Beckingham, L. E., Steefel, C. I., Swift, A. M., et al. Evaluation of accessible mineral surface areas for improved prediction of mineral reaction rates in porous media. *Geochimica et Cosmochimica Acta*, 2017, 205: 31-49.
- Bethke, C. M. *Geochemical and Biogeochemical Reaction Modelling*. Cambridge, UK, Cambridge University Press, 2008.
- Black, J. R., Haese, R. R. Chlorite dissolution rates under CO<sub>2</sub> saturated conditions from 50 to 120 °C and 120 to 200 bar CO<sub>2</sub>. *Geochimica et Cosmochimica Acta*, 2014, 125: 225-240.
- Blondes, M. S., Gans, K. D., Engle, M. A., et al. *U. S. Geological Survey National Produced Waters Geochemical Database (ver. 2.3, January 2018)*. U.S. Geological Survey data release, 2018.
- Daval, D., Martinez, I., Corvisier, J., et al. Carbonation of Ca-bearing silicates, the case of wollastonite: Experimental investigations and kinetic modeling. *Chemical Geology*, 2009, 265(1-2): 63-78.

- Delany, J. M., Lundeen, S. R. The LLNL Thermochemical Database. San Francisco, Lawrence Livermore National Laboratory Report UCRL-21658, 1990.
- Emmanuel, S. Modeling the effect of mineral armoring on the rates of coupled dissolution-precipitation reactions: Implications for chemical weathering. *Chemical Geology*, 2022, 601: 120868.
- Fetter, C. W. *Applied Hydrogeology* Fourth Edition. USA, Pearson Education Limited, 2014.
- Folk, R. L. *Petrology of Sedimentary Rocks*. Texas, Hemphill Publishing Company, 1974.
- Giles, M. R. Mass transfer and problems of secondary porosity creation in deeply buried hydrocarbon reservoirs. *Marine and Petroleum Geology*, 1987, 4(3): 188-204.
- Golubev, S. V., Bénézeth, P., Schott, J., et al. Siderite dissolution kinetics in acidic aqueous solutions from 25 to 100 °C and 0 to 50 atm  $p\text{CO}_2$ . *Chemical Geology*, 2009, 265(1-2): 13-19.
- Gong, L., Gao, X., Qu, F., et al. Reservoir quality and controlling mechanism of the Upper Paleogene fine-grained sandstones in lacustrine basin in the hinterlands of Northern Qaidam Basin, NW China. *Journal of Earth Science*, 2023, 34: 806-823.
- Helgeson, H. C. Thermodynamics of hydrothermal systems at elevated temperatures and pressures. *American Journal of Science*, 1969, 267(7): 729-804.
- Helgeson, H. C., Knox, A. M., Owens, C. E., et al. Petroleum, oil field waters, and authigenic mineral assemblages: Are they in metastable equilibrium in hydrocarbon reservoirs? *Geochimica et Cosmochimica Acta*, 1993, 57(14): 3295-3339.
- Higgs, K. E., Haese, R. R., Golding, S. D., et al. The Pretty Hill Formation as a natural analogue for  $\text{CO}_2$  storage: An investigation of mineralogical and isotopic changes associated with sandstones exposed to low, intermediate and high  $\text{CO}_2$  concentrations over geological time. *Chemical Geology*, 2015, 399: 36-64.
- Hodson, M. E. The influence of Fe-rich coatings on the dissolution of anorthite at pH 2.6. *Geochimica et Cosmochimica Acta*, 2003, 67(18): 3355-3363.
- Hurst, A., Nadeau, P. H. Clay microporosity in reservoir sandstones: An application of quantitative electron microscopy in petrophysical evaluation. *AAPG Bulletin*, 1995, 79(4): 563-573.
- Kharaka, Y. K., Cole, D. R., Hovorka, S. D., et al. Gas-water-rock interactions in Frio Formation following  $\text{CO}_2$  injection: Implications for the storage of greenhouse gases in sedimentary basins. *Geology*, 2006, 34(7): 577-580.
- Lammers, K., Smith, M. M., Carroll, S. A. Muscovite dissolution kinetics as a function of pH at elevated temperature. *Chemical Geology*, 2017, 466: 149-158.
- Lander, R. H., Walderhaug, O. Predicting porosity through simulating sandstone compaction and quartz cementation. *AAPG Bulletin*, 1999, 83(3): 433-449.
- Lasaga, A. C. *Kinetic Theory in the Earth Sciences*. Princeton, Princeton University Press, 2014.
- Li, H., Hu, Q., Jones, S., et al. A review and discussion on the influences of grain-coating clay minerals on water-rock interactions in sandstones. *Earth-Science Reviews*, 2025, 263: 105073.
- Li, H., Hu, Q., Wang, F., et al. Alteration of chlorite coats and sandstone porosity reduction: Insights from reactive transport modelling. *Marine and Petroleum Geology*, 2024, 160: 106641.
- Luhmann, A. J., Kong, X. Z., Tutolo, B. M., et al. Experimental dissolution of dolomite by  $\text{CO}_2$ -charged brine at 100 °C and 150 bar: Evolution of porosity, permeability, and reactive surface area. *Chemical Geology*, 2014, 380: 145-160.
- Luquot, L., Andreani, M., Gouze, P., et al.  $\text{CO}_2$  percolation experiment through chlorite/zeolite-rich sandstone (Pretty Hill Formation-Otway Basin-Australia). *Chemical Geology*, 2012, 294-295: 75-88.
- McKinley, J. M., Worden, R. H., Ruffell, A. H. Smectite in sandstones: A review of the controls on occurrence and behaviour during diagenesis, in *Clay Mineral Cements in Sandstones*, edited by R.H. Worden and S. Morad, International Association of Sedimentologists Special Publication 34, pp. 109-128, 2003.
- Metz, B., Davidson, O., de Coninck, H., et al. *IPCC Special Report on Carbon Dioxide Capture and Storage*. Cambridge and New York, Cambridge University Press, 2005.
- Oelkers, E. H., Schott, J., Devidal, J. L. The effect of aluminum, pH, and chemical affinity on the rates of aluminosilicate dissolution reactions. *Geochimica et Cosmochimica Acta*, 1994, 58(9): 2011-2024.
- Palandri, J. L., Kharaka, Y. K. *A Compilation of Rate Parameters of Water-Mineral Interaction Kinetics for Application to Geochemical Modeling*. No. OPEN-FILE-2004-1068. California, U.S. Geological Survey, 2004.
- Park, A. J. Water-rock interaction and reactive-transport modelling using elemental mass-balance approach: I. The methodology. *American Journal of Science*, 2014, 314(3): 785-804.
- Pokrovsky, O. S., Golubev, S. V., Schott, J., et al. Calcite, dolomite and magnesite dissolution kinetics in aqueous solutions at acid to circumneutral pH, 25 to 150 °C and 1 to 55 atm  $p\text{CO}_2$ : New constraints on  $\text{CO}_2$  sequestration in sedimentary basins. *Chemical Geology*, 2009, 265(1-2): 20-32.
- Rosenqvist, J., Kilpatrick, A. D., Yardley, B. W. D., et al. Alkali feldspar dissolution in response to injection of carbon dioxide. *Applied Geochemistry*, 2019, 109: 104419.
- Schulz, H. D., Zabel, M. *Marine Geochemistry*. Berlin, Heidelberg, Springer-Verlag, 2006.
- Walderhaug, O., Porten, K. W. How do grain coats prevent formation of quartz overgrowths? *Journal of Sedimentary Research*, 2022, 92(10): 988-1002.
- Worden, R. H., Griffiths, J., Wooldridge, L. J., et al. Chlorite in sandstones. *Earth-Science Reviews*, 2020, 204: 103105.
- Xu, M. J., Eckstein, Y. Use of weighted least-squares method in evaluation of the relationship between dispersivity and field scale. *Groundwater*, 1995, 33(6): 905-908.